Research Highlights

Life Science

Bacterial Diterpene Synthases: A Tale of Two Conserved Domains

This report features the work of Rey-Ting Guo, Eric Oldfield and their co-workers published in J. Am. Chem. Soc. ***136****, 2892 (2014) and Sci. Rep.* ***4****, 6214 (2014).*

Terpenes (or terpenoids) represent the largest class of small molecules on the planet. About 20% of terpenes are diterpenes, molecules that contain a core of 20 carbon atoms, and most are made by plant and fungal enzymes. Diterpenes are, however, also found in bacteria, and several of these compounds have activity as anti-infective and anti-cancer drug leads and virulence factors, as well as plant growth hormones.

The structures and mechanism of action of terpene synthases have been studied for many years, but the first structures of diterpene synthases were unreported until 2011.[1,2] These are two diterpene cyclases from plants and adopt an "αβγ" three-helical conserved domain structure.[1,2] It was proposed that the plant αβγ domain proteins arose by fusion of the genes of ancestral α and βγ domain synthases in soil-dwelling bacteria, but no structures of bacterial diterpene synthases have been reported.

To understand bacterial diterpene synthases better, Rey-Ting Guo, Eric Oldfield and their co-workers solved two bacterial diterpene synthase structures: virulence-associated enzyme (Rv3378c) from *Mycobacterium tuberculosis*[3] and *ent*-kaurene synthase (BjKS) from soil bacterium *Bradyrhizobium japonicum*.[4] The former protein is of interest as its product (1-tuberculosinyl adenosine) is a virulence factor for *M. tuberculosis*, and, hence, targets for anti-virulence-based therapies.[5] The latter is of interest as it is involved in gibberellin biosynthesis; its structure serves as a test of the hypothesis that the αβγ-domain in plant αβγ diterpene synthases might have arisen from a bacterial diterpene synthase. Their work used **BL13B1**, **BL13C1** and **BL15A1** at the TLS.

Rv3378c catalyzed the condensation of adenosine and TPP to generate 1-TbAd (Fig. 1(a)).[5] The crystal structures of Rv3378c in apo-form and in a complex with its substrate TPP were solved here (Figs. 1(b) and 1(c)). These workers obtained also Rv3378c in a complex with a bisphosphonate inhibitor (BPH-629), in which one molecule occupied the TPP substrate-binding site and a second is located at the dimer interface (Fig. 2). These structures will help guide further antibiotic design against *M. tuberculosis*.

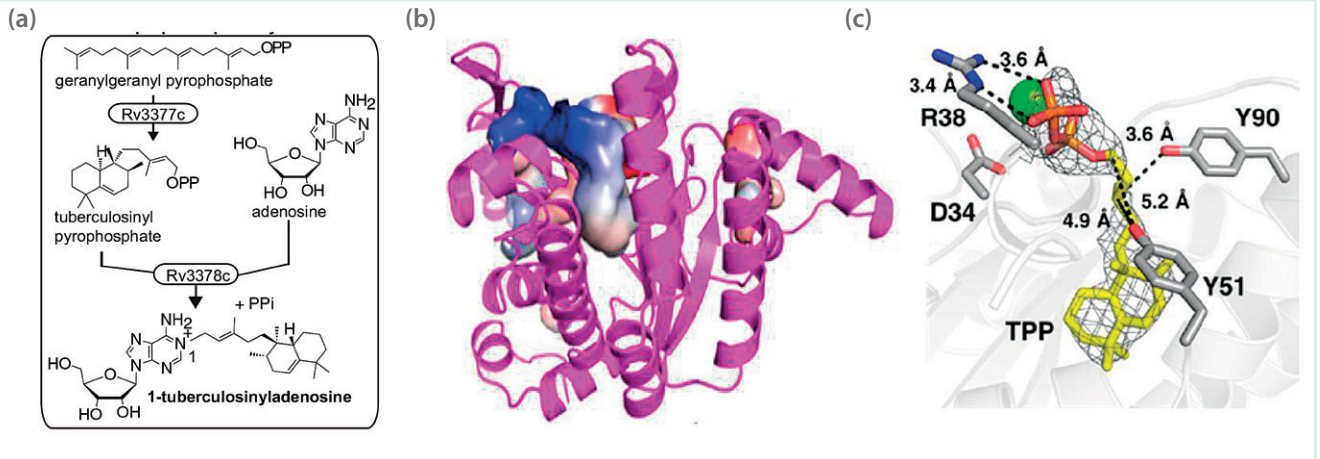

Fig. 1: Structures of Rv3378c. (a) Catalysis of Rv3378c. (b) Rv3378c ligand binding site. (c) Rv3378c/TPP (yellow, electron density contoured at 1.5σ) complex structure.

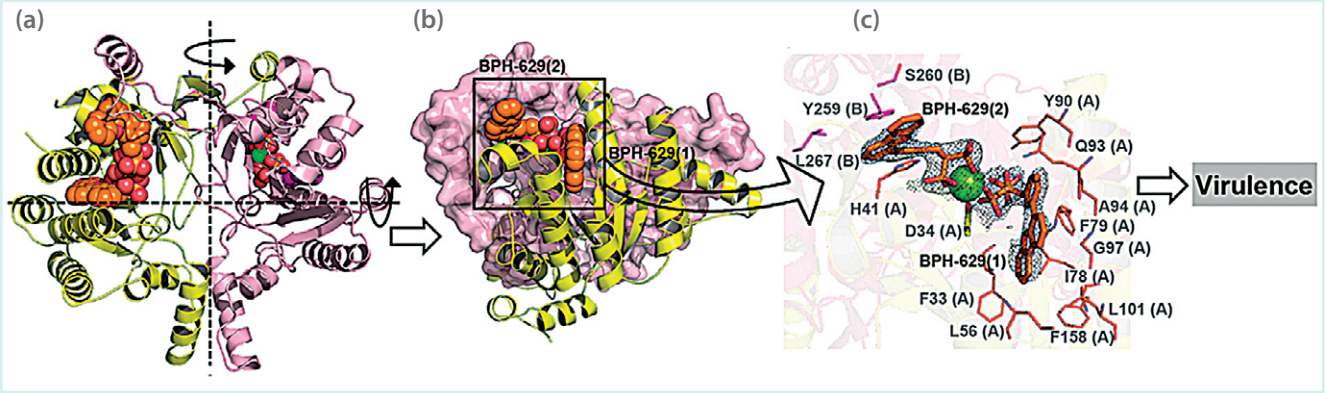

Fig. 2: Inhibitor-bound structures of Rv3378c. (a) Dimeric Rv3378c structure with four bound BPH-629 molecules. (b) Front view of Rv3378c dimer. (c) Close-up view of the structure of Rv3378c bound to bisphosphonate inhibitor BPH-629.

The structure of BjKS is similar to that found in the α domain in plant diterpene cyclases, indicating that modern plant terpene cyclases might have arisen from a fusion of the genes of ancestral (bacterial) α and βγ domain proteins. In addition, the structure of a diterpene diphosphate (*ent*-copalyl diphosphate) bound to a diterpene cyclase helps define the diterpene cyclase substrate-binding site (Fig. 3(a)). Three residues D75, D79 and R204 are confirmed to be essential for catalysis on using site-directed mutagenesis (Fig. 3(b) and 3(c)). The same aromatic bisphosphonate inhibitor used for the study of Rv3378c (BPH-629) was found to bind in the *ent*-CPP diphosphate-binding site and thus might be used as a potential plant-growth regulator (Fig. 3(d)).

References

1. M. Koksal, H. Hu, R. M. Coates, R. J. Peters, and D. W. Christianson, Nat. Chem. Biol. **7**, 431 (2011).
2. M. Koksal, Y. Jin, R. M. Coates, R. Croteau, and D. W. Christianson, Nature **469**, 116 (2011).
3. H. C. Chan, X. Feng, T. P. Ko, C. H. Huang, Y. Hu, Y. Zheng, S. Bogue, C. Nakano, T. Hoshino, L. Zhang, P. Lv, W. Liu, D. C. Crick, P. H. Liang, A. H. Wang, E. Oldfield, and R. T. Guo, J. Am. Chem. Soc. **136**, 2892 (2014).
4. W. Liu, X. Feng, Y. Zheng, C. H. Huang, C. Nakano, T. Hoshino, S. Bogue, T. P. Ko, C. C. Chen, Y. Cui, J. Li, I. Wang, S. T. Hsu, E. Oldfield, and R. T. Guo, Sci. Rep. **4**, 6214 (2014).
5. E. Layre, H. J. Lee, D. C. Young, A. J. Martinot, J. Buter, A. J. Minnaard, J. W. Annand, S. M. Fortune, B. B. Snider, I. Matsunaga, E. J. Rubin, T. Alber, and D. B. Moody, Proc. Natl. Acad. Sci. USA **111**, 2978 (2014).

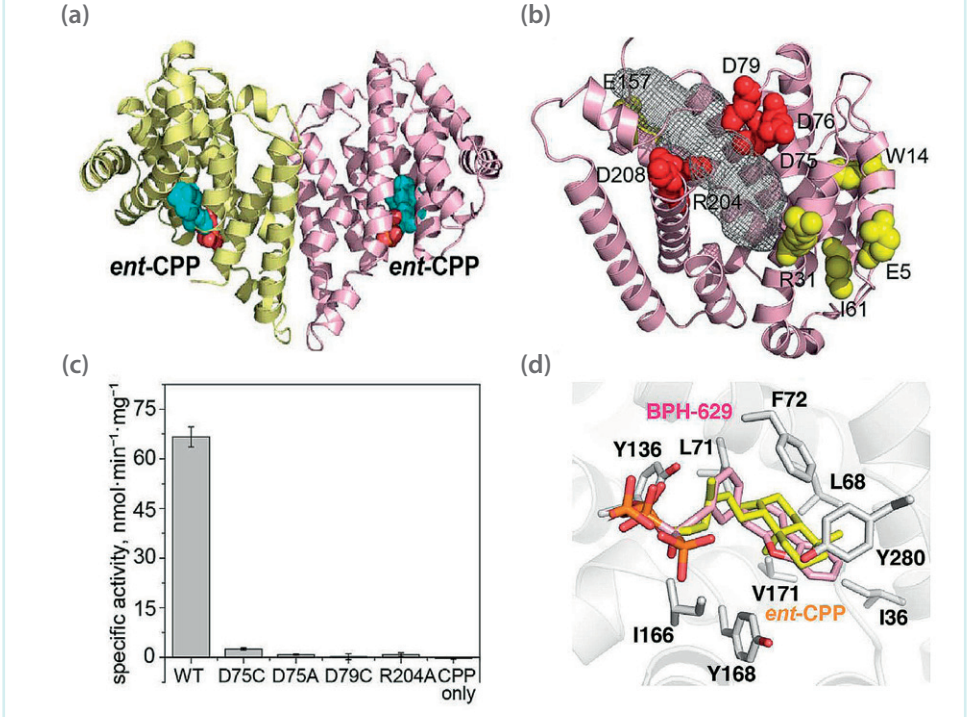

Fig. 3: Binding site, essential residues, and inhibition. (a) Stereo-view of *ent*-CPP bound structure (PDB ID 3WBV). (b) Highly conserved residues; residues in red mutated to A or C. (c) Activity of wild-type and mutant proteins. (d) Stereo-view of *ent*-CPP and BPH-629 in the BjKS active site.

Developing Novel Antibiotics to Kill Vancomycin-Resistant Enterococcus

This report features the work of Syue-Yi Lyu, Tsung-Lin Li and their co-workers published in J. Am. Chem. Soc. ***136****, 10989 (2014).*

Lipoglycopeptide antibiotic teicoplanin A2-2 **1** (Tei)/A40926 **2** carries a unique long aliphatic acyl side chain attached to glucosamine at the central residue of the Tei/A40926 pseudoaglycone scaffold **3** (Fig. 1). The gene products *orf11** and *dbv8* were characterized to be *N*-acyltransferases (NAT) responsible for *N*-acylation in the biosynthesis of Tei/A40926.[1] This modification endows the lipoglycopeptide antibiotic with an ability to exterminate multidrug-resistant Gram-(+) pathogens, e.g. methicillin-resistant *Staphylococcus aureus* and vancomycin-resistant enterococcus (VRE).[2,3] New applications of the enzyme have since been implied but without elaboration and detail.[4] It is thus of great interest to understand how two bulky substrates, Tei/A40926 pseudoaglycone **3** and decanoyl-CoA **4**, are recruited and how the acyl-transfer reaction is executed. To address these questions, Tsung-Lin Li and his co-workers at Academia Sinica pursued the complicated structures of NAT at various stages of reaction using BL13B1 and BL13C1 at the TLS and BL12B2 at SPring-8. In parallel with the structural determination, the authors discovered two unusual acyl-transfer reactions, providing a new chemoenzymatic strategy to obtain products in new classes that would be extremely difficult to obtain by other means, and that offer improved and complementary profiles for antimicrobial drug discovery efforts.

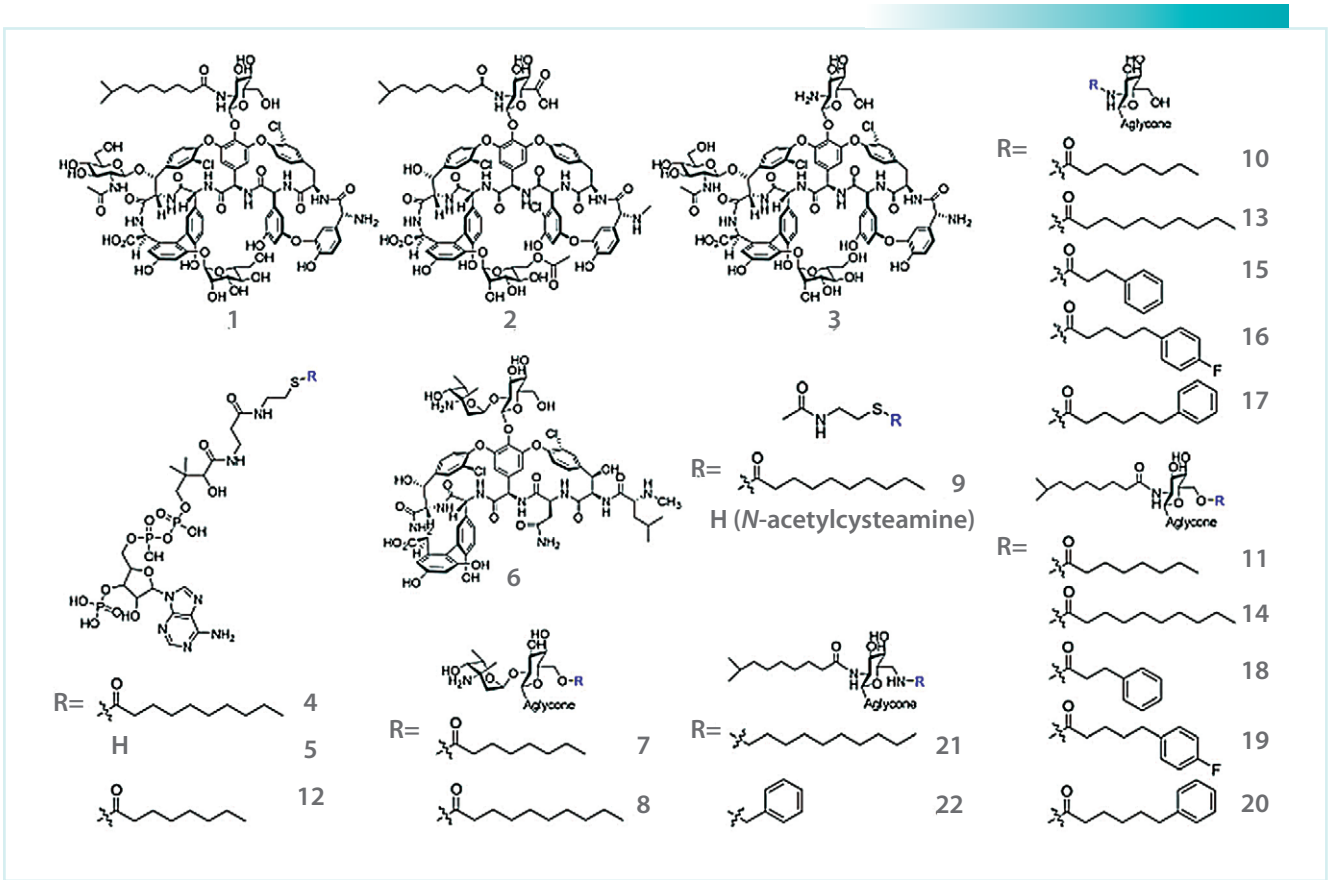

Fig. 1: Chemical structures of glycopeptides, acyl-*N*-acetyl cysteamine, and CoA derivatives.

The authors first presented eight high-resolution X-ray crystallographic unary, binary and ternary complexes to decipher the molecular basis for the functionality of NAT. Both Orf11* and Dbv8 fold in a dumbbell-like architecture, with two sizable subdomains—an unusual all-helix N-domain and a GNAT-like C-domain. Superimposition of the ligand-free and ligand-bound structures revealed that the enzyme undergoes a multistage conformational change upon binding of acyl-CoA, thus allowing the uploading of Tei pseudoaglycone to enable the acyl-transfer reaction to occur in the occlusion between the N- and C-halves of the protein.

The authors further demonstrated that Orf11*/Dbv8 is an adaptable enzyme that can generate numerous new glycopeptide analogues. The acyl moiety of acyl-CoA can be bulky or lengthy, allowing much diversity in new derivatives that can be formed upon its transfer. Interestingly, vancomycin **6** and synthetic acyl-*N*-acetyl cysteamine **9** were not expected to be able to serve as surrogates for an acyl acceptor and donor, respectively.

It has been well documented that the acyl transfer can proceed in two ways, a direct transfer and an acyl-enzyme mediated transfer as seen in histone AT. Three reaction states—pre-acylation, tetrahedral intermediate and post-acylation—were spotted in three individual ternary structures (Fig. 2), indicating that the acyl transfer of Orf11*/Dbv8 follows the direct transfer mechanism. In brief, the H196 acts as a general base deprotonating the C2 NH^{3+} of glucosamine at 4Hpg, which then attacks the thioester carbonyl carbon of acyl-CoA. The resulting tetrahedral transition structure is stabilized by the main-chain amide of V197, in which an oxyanion hole likely resides. Collapse of the transition structure results in *N*-acylated Tei pseudoaglycone. The departure of CoASH might be facilitated by S236 through protonating the sulfur anion to sulfhydryl (Fig. 2). This mechanistic notion was supported by mutagenic and biochemical assays, as relative activities of mutants H196A and H196A/S236A plunged significantly (5% and 0%, respectively, relative to WT).

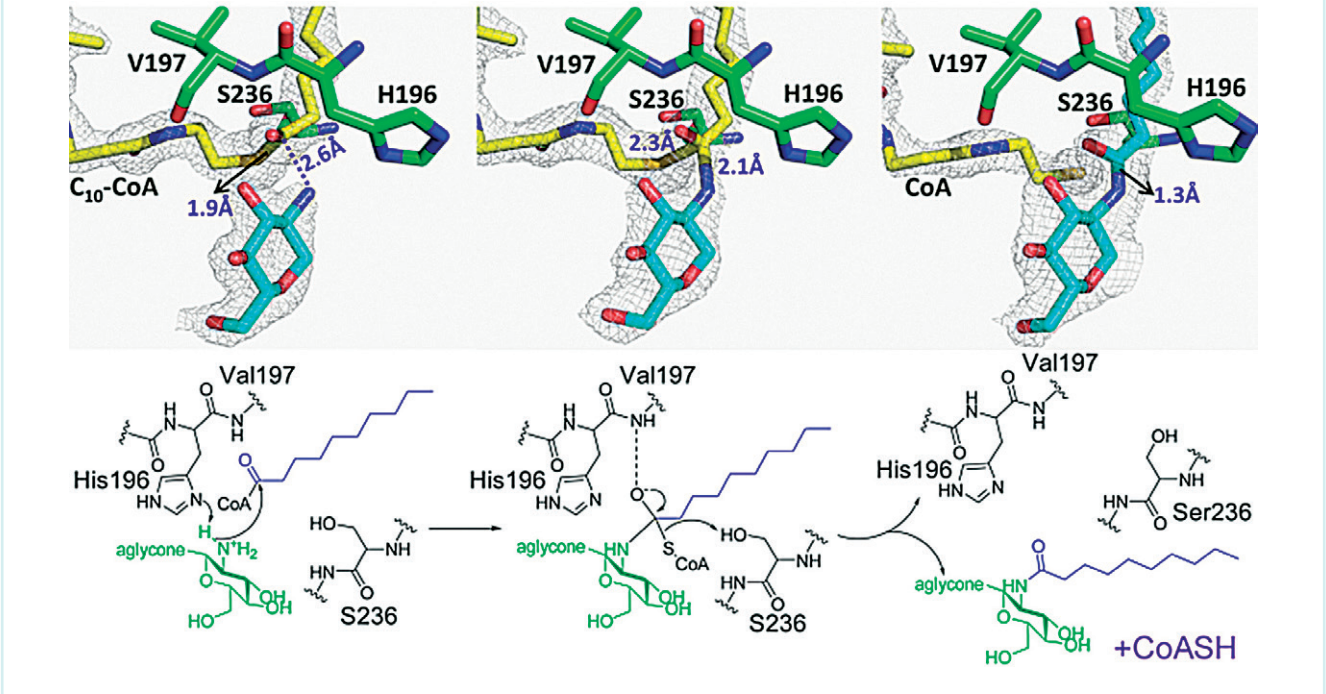

Fig. 2: Reaction intermediates and proposed enzymatic mechanisms.

Most strikingly, a double-acylation reaction and an acyl-substitution reaction were discovered, whereby Tei **1** becomes converted to C_8-Tei **10** and C_8, C_{10}-Tei **11** in an enzyme reaction containing Tei **1** and octanoyl-CoA **12**. The authors reasoned that the *2N,6O*-diacyl glucosamine moiety subject to intramolecular restraints under the active site constraints experiences an equatorial-axial interconversion via a twist-boat state. In a 1,4-diaxial fashion (a boat conformation) the C6 acyl and the C2 secondary amine are within a bond-length distance allowing a C6⟶C2 acyl migration to form a germinal diacyl intermediate. Given that the migrated acyl moiety likely remains inside a lipid tunnel, the solvent-exposed C2-*N*-acyl group is more accessible to water attack, thus resulting in formation of the acyl-substituted Tei. Two additional crystal structures were solved to verify this working model. The electron densities for both the C2-*N*-acyl and aglycone moieties were too faint to be modeled, likely due to large molecular oscillation, whereas the electron density of the glucosamine moiety was well defined, with the C6 OH clearly pointing to the acyl-CoA carbonyl carbon in one structure and with formation of a C6-*O*-acyl bond in the other, supporting the first two stages in the working model (Fig. 3).

The authors proceeded to examine the reaction conditions in a bid to control the reaction. One set of conditions (pH 7.0, 1 molar equiv of acyl-NAC/Tei) gives ratio 4:1 for acyl-substituted Tei versus diacyl Tei; the ratio is reversed (1:4) in another set of conditions (pH 9.0, 3 molar equiv of acyl-NAC/Tei, 30% DMSO). Overall, the conversion is a mild and effective one-step reaction, of which the final yield is large because the minor product is recyclable in each condition. The authors reasoned that the reaction mechanism is a synergy of stoichiometric and solvational effects. This work affords an expedient way to generate new Tei analogues without problematic deacylation and reacylation processes.[4,5] This finding also provides a one-pot solution to convert Tei mixtures of natural isolates to a single uniform compound, which

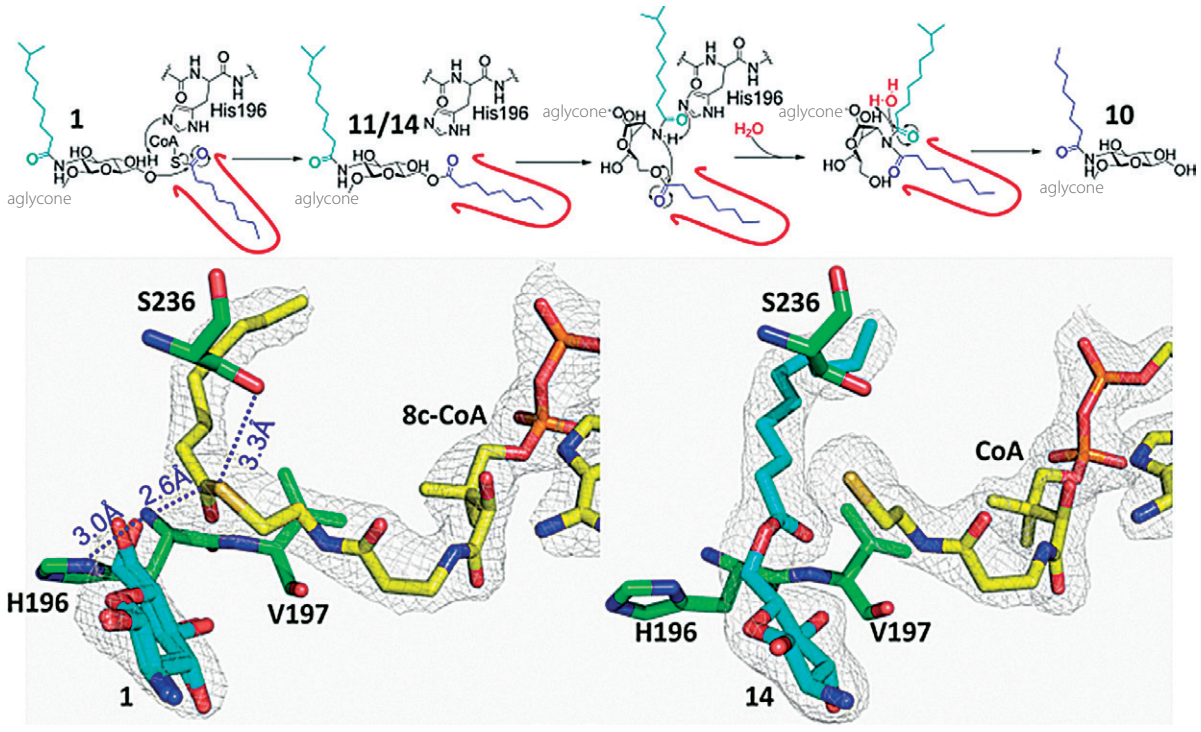

Fig. 3: Proposed mechanism of Orf11*-mediated 1,4-acyl-migration reaction. The lipid tunnel in Orf11* is schematized in red. Bottom panel: structural views for the first two acyl-migration reaction states.

should facilitate the development of approvable drugs (teicoplanin in mixtures is one reason that it is not approved by the USA FDA).

Having added new chemical functionality with the modified Tei analogues, the authors sought to examine whether they had similarly expanded new biological functionality; accordingly, the authors determined the minimum inhibition concentrations of several compounds against collections of major types (VanABC) of VRE. The 2*N*,6*O*-diacyl analogues (**11**, **18**, **19**, **20**) showed significantly enhanced bactericidal activities against all nine tested strains (both sensitive and resistant strains) when compared with mono *N*-acyl-substituted Tei, vancomycin and teicoplanin. On investigating the bactericidal variations among these diacyl analogues, the authors found that straight-chain octanoyl analogue **11** slightly outperformed phenylpropionyl analogue **18**, which, however, is compensated on increasing the chain length (analogues **19** and **20**). VanC VRE is more sensitive to analogue **19**, wherein the fluorine substituent at the *para* position of the phenyl ring might exert some electronic influence; both straight-chain analogue **11** and phenylhexanoyl analogue **20** are more effective against VanA VRE.

The development of new antibiotics with enhanced or broadened antimicrobial efficacy remains a pressing and challenging goal. Elucidation of the key long-aliphatic *N*-acyltransferase complexes in the biosynthesis of the clinically important antibiotic teicoplanin/A40926 not only resolved the difficult problems but also expanded the ordinary task of the enzyme. The authors expect that the broad-substrate acyl-transfer, diacyl- transfer and acyl-substitution reactions identified will offer a valuable way to make more effective and synthetically challenging biochemicals to meet strong synthetic and medicinal demands.

References

1. S. Y. Lyu, Y. C. Liu, C. Y. Chang, C. J. Huang, Y. H. Chiu, C. M. Huang, N. S. Hsu, K. H. Lin, C. J. Wu, M. D. Tsai, and T. L. Li, J. Am. Chem. Soc. **136**, 10989 (2014).
2. D. Kahne, C. Leimkuhler, W. Lu, and C. Walsh, Chem. Rev. **105**, 425 (2005).
3. T. L. Li, F. Huang, S. F. Haydock, T. Mironenko, P. F. Leadlay, and J. B. Spencer, Chem. Biol. **11**, 107 (2004).
4. Y. C. Liu, Y. S. Li, S. Y. Lyu, L. J. Hsu, Y. H. Chen, Y. T. Huang, H. C. Chan, C. J. Huang, G. H. Chen, C. C. Chou, M. D. Tsai, and T. L. Li, Nat. Chem. Biol. **7**, 304 (2011).
5. H. C. Chan, Y. T. Huang, S. Y. Lyu, C. J. Huang, Y. S. Li, Y. C. Liu, C. C. Chou, M. D. Tsai, and T. L. Li, Mol. Biosyst. **7**, 1224 (2011).

New Directions for Therapeutic Treatment of Colorectal Cancer

*This report features the work of Kai-En Chen, Tzu-Ching Meng, Andrew H.-J. Wang and their co-workers published in Sci. Signal. **7**, ra98 (2014).*

The Ras signaling cascade has long been considered an attractive therapeutic target for colorectal cancer (CRC). Among the modules in this signaling pathway, p38γ and its specific phosphatase PTPN3 are known to be the key regulator responsible for Ras-mediated oncogenic activity. Recent attention has been drawn to the PDZ-mediated PTPN3-p38γ complex, which is known to be a novel target for Ras-dependent malignancies, but the dynamic nature of the phosphatase-kinase interactions have so far resisted efforts by structural biologists to explore the detailed molecular insight of drug targets in this important group. In 2014, a research team led by Andrew H.-J. Wang and Tzu-Ching Meng from Academia Sinica determined this complex with a hybrid method combining X-ray crystallography, small-angle X-ray scattering (SAXS) and chemical cross-linking coupled with mass spectrometry (CX-MS). The structure demonstrated the formation of an active-state complex and the unique

regulatory role of the PDZ domain of PTPN3.

Mitgoen-activated protein kinases (MAPK) are composed of four isoforms—p38α, p38β, p38γ and p38δ. p38γ differs from other p38 MAPK by the presence of a C-terminal ETPL motif,[1] which binds to the PDZ domain in interacting proteins. Previous work has shown that p38γ and its specific phosphatase PTPN3 (PTPH1) cooperate through the PDZ domain to promote Ras transformation in human cancers.[2] To investigate the molecular basis of the interaction between PTPN3 and p38γ, the research team used advanced X-ray techniques in the TLS, including protein crystallography beamline **BL15A1** and small and wide-angle X-ray scattering beamline **BL23A1**.

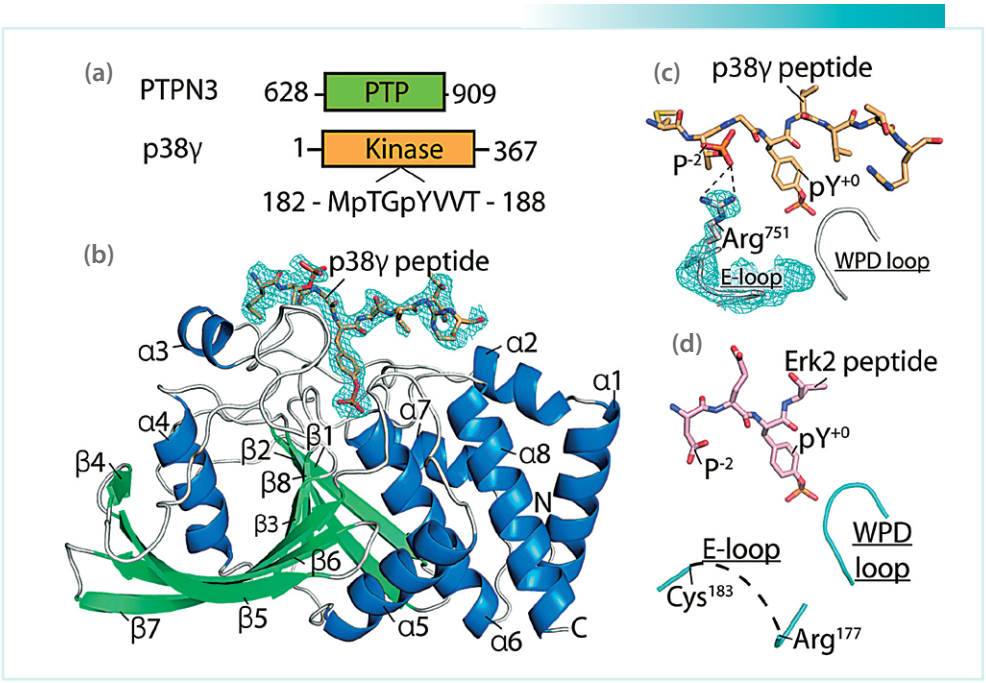

Fig. 1: Crystal structure of PTPN3 PTP domain D811A/C842S mutant in a complex with dually phosphorylated peptide p38γ. (a) Schematic showing the constructs of PTPN3 and p38γ. (b) Representation of the complex structure (PDB ID: 4QUM). (c) Active site of the complex structure highlights the interaction between Arg^{751} and $pThr^{183}$ (P^{-2}). (d) Active site of HePTP in the complex with the Erk2 mimetic peptide (PDB ID: 3D44). The electron density shown corresponds to a simulated-annealing OIMT F_o-F_c map contoured at 3σ. (Modified from Ref. 4)

In this work, the crystal structure of the PTPN3 PTP catalytic domain in a complex with dually phosphorylated peptide p38γ that mimics the TxY motif of the activation loop (Fig. 1(a)) was determined at 2.5-Å resolution. The structure revealed a monomer in the asymmetric unit with p38γ phosphopeptide clearly visible in the complex structure (Fig. 1(b)). According to Figs. 1(c) and 1(d), the unique feature in this complex structure is the salt bridge interaction between the phosphate oxygen of P^{-2}($pThr^{183}$ of p38γ) and nitrogen atoms of the guanidine group of Arg^{751} in the E-loop of PTPN3. In comparison with the structure of HePTP in a complex with a phosphorylated Erk2 peptide, such a salt bridge does not exist. Together with kinetic and mutagenesis data, this work indicates that PTPN3 prefers to recognize dually phosphorylated ($pThr^{183}$-Gly-$pTyr^{185}$) rather than mono-phosphorylated (Thr-Gly-$pTyr^{185}$) p38γ as a substrate.

To extend these findings, the research team applied SAXS to investigate whether PTPN3 and p38γ protein-protein complex in solution can support an active-state binding mode. As shown in Fig. 2(a), the pair distance-distribution plot indicated that the complex had a globular shape in solution, with D_{max} = 91 Å and R_g = 28.5 Å. The structure *ab initio* of the complex, calculated with DAMMIN, also revealed a compact shape similar to the active-state envelope of PTP-MPAK complexes published previously[3] (Fig. 2(b)). Using the FoXS calculation, the research team found that the active site pocket of PTPN3 was in close proximity to the activation loop of protein p38γ (Fig. 2(c)). The agreement between solution and crystal structure indicates that the active-state complex is the dominant form when PTPN3 recognizes p38γ.

Next, the research team applied the CX-MS ap-

proach to map the PDZ domain arrangement in the active-state complex. As shown in Fig. 3(a), three lysine residues (Lys^{520}, Lys^{526} and Lys^{532}) of the PDZ domain of PTPN3 were cross-linked with either Lys^{352} or Lys^{363} located on the C-terminal ETPL motif of dually phosphorylated p38γ protein.

In the absence of p38γ, the PDZ and PTP domains of PTPN3 form a unique intramolecular cross-linking that was not detected in the active-state complex. According to the distance restraint of the BS3 cross-linker, the PDZ and PTP domains are believed to form a compact conformation in the absence of p38γ (Figs. 3(b) and 3(c)). Together, the findings from this work indicate two new directions for a rational drug design to target human cancers, especially CRC, in which PTPN3 is highly expressed and expected to promote Ras oncogenic signaling through dephosphorylation of p38γ.

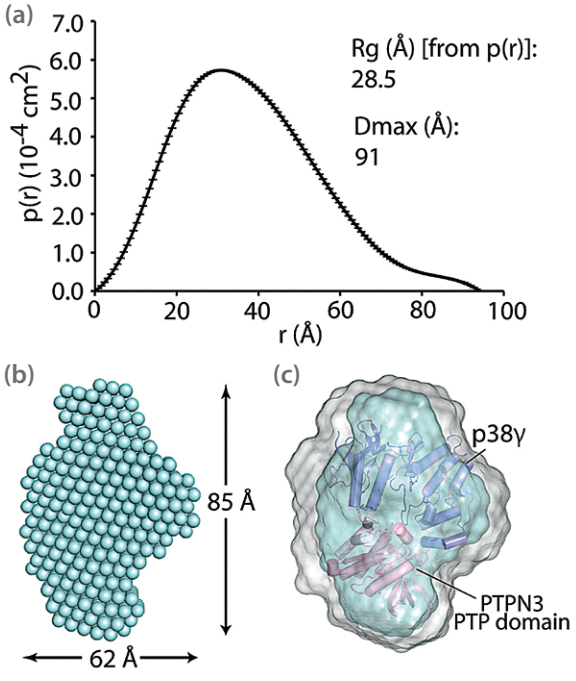

Fig. 2: SAXS data and model of the PTPN3-p38γ complex *ab initio* (a) Pair distance-distribution plots derived from the experimental scattering data using GNOM. (b) Probable shape of the complex obtained with an averaging and filtering process from program DAMAVER. (c) Envelope *ab initio* overlaid with the optimized models of the complex calculated from FoXS. (Modified from Ref. 4)

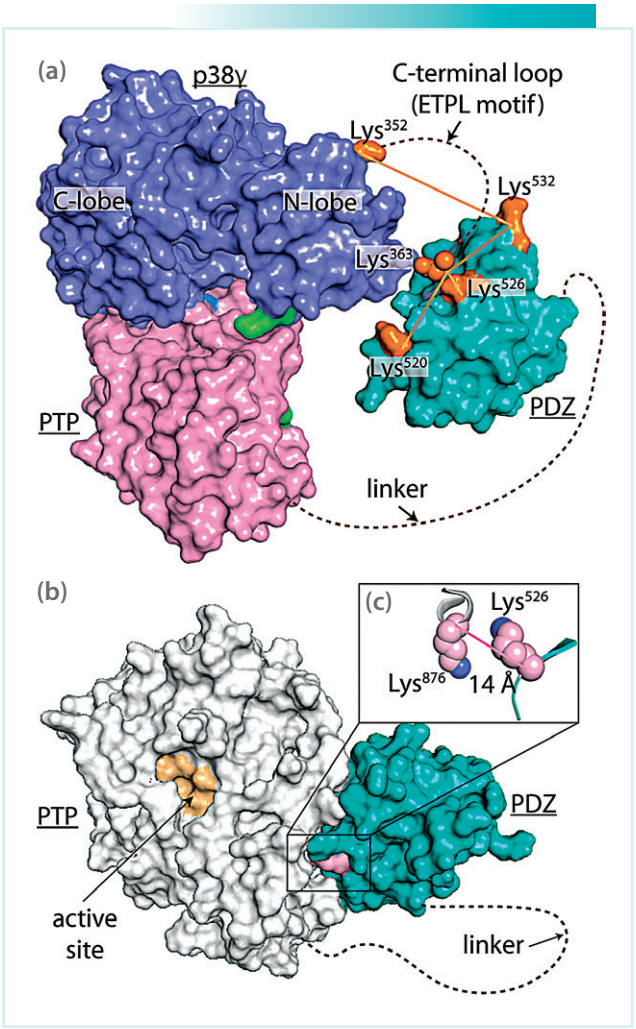

Fig. 3: CX-MS based assembly of the PTPN3 - p38γ complex. (a) Complex model with the PDZ domain attached near the N-lobe of p38γ. (b) Model structure of PTPN3 to show the close proximity of the PDZ and PTP domains. (c) Enlarged view showing the cross-linking pair. (Modified from Ref. 4)

References

1. M. Hasegawa, A. Cuenda, M. G. Spillantini, G. M. Thomas, V. Buée-Scherrer, P. Cohen, and M. Goedert, J. Biol. Chem. **274**, 12626 (1999).
2. S. W. Hou, H. Y. Zhi, N. Pohl, M. Loesch, X. M. Qi, R. S. Li, Z. Basir, and G. Chen, Cancer Res. **70,** 2901 (2010).
3. D. M. Francis, G. S. Kumar, D. Koveal, A. Tortajada, R. Page, and W. Peti, Structure **21**, 1612 (2013).
4. K.-E. Chen, S.-Y. Lin, M.-J. Wu, M.-R. Ho, A. Santhanam, C.-C. Chou, T.-C. Meng, and A. H.-J. Wang, Sci. Signal. **7**, ra98 (2014).

Resolving the Phase Ambiguity of Single-Wavelength Anomalous Dispersion

This report features the work of Chun-Jung Chen and his co-workers published in Acta Cryst. ***D70****, 2331 (2014).*

X-ray protein crystallography remains a predominant method in the community to determine the three-dimensional structures of biological macromolecules. Despite great progress towards its automation and efficiency, phasing massive diffraction reflections remains a critical step for the determination of structures. The importance of the single-wavelength anomalous dispersion (SAD) method using sulfur and various heavy atoms in proteins in the phasing purpose has increased because protein crystals are typically damaged by synchrotron radiation during the long duration of data collection with the commonly used multiple-wavelength anomalous-dispersion method.[1,2] Two possible phase solutions (ϕ_1 and ϕ_2) generated from two symmetric phase triangles in the Harker construction for the SAD method cause the well-known phase ambiguity (Fig. 1).

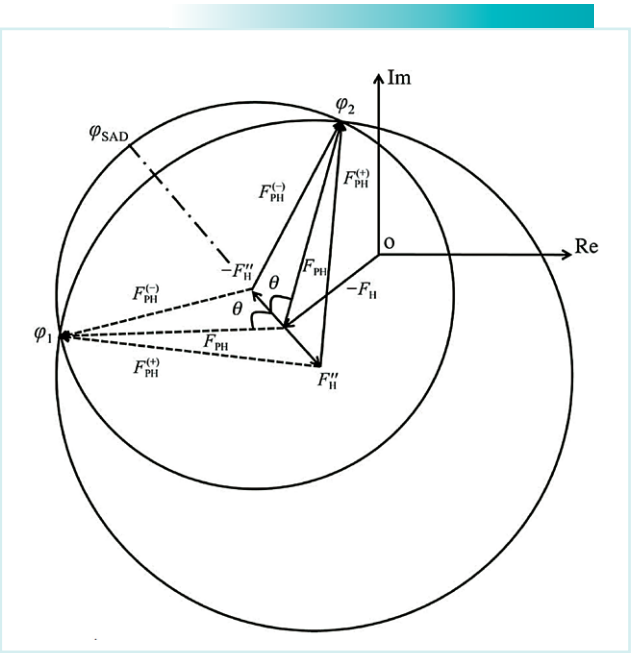

Fig. 1: Harker construction for SAD phasing. The contribution of heavy atoms to a structure factor consists of a normal part, F_H, and an anomalous part, F''_H. The structure factor F_{PH} is a normal part and F^+_{PH} and F^-_{PH} are anomalous parts from a protein crystal containing heavy atoms. (Reproduced from Ref. 3)

In 2014, a research team of Chun-Jung Chen from the Life Science Group, NSRRC, developed a novel algorithm to optimize the initial phases from the SAD.[3] This so-called direct phase-selection method greatly enhances the success of the subsequent electron-density modification, model building and structure determination of biological macromolecules, which will benefit the community of structural biology.

This newly developed algorithm can effectively improve the initial phases from the general SAD method with sulfur or heavy atoms using a novel direct phase-selection method based on a θ_{DS} list; θ_{DS} is the angle between the initial SAD phase and the preliminary DM phase, differing from previously reported methods. The authors demonstrated that this method of phase selection can resolve the phase ambiguity and improve the phases from SAD with increased effectiveness in combination with *RESOLVE* or *DM* utilizing only simple solvent flattening without phase combination and a FOM cutoff. They tested several experimental SAD data sets with sulfur or metal (Zn, Gd, Fe and Se) atoms as the anomalous scatterers, which were collected at protein crystallography beamlines, including **BL13B1** and **BL15A1** at the TLS and **BL12B2** and **BL44XU** at SPring-8. All results showed superior phases to generate electron-density maps with an enhanced quality and model building with greater completeness.

Their work showed that a high percentage correct for the SAD phases occurs at angle θ_{DS} in a range 35–145° in region 1 or 2, respectively (Fig. 2). The "θ_{DS} list" from the smallest to the largest angles can be generated. Reflections from the θ_{DS} list with angle θ_{DS} between 35° and 145° are selected, which have a large probability

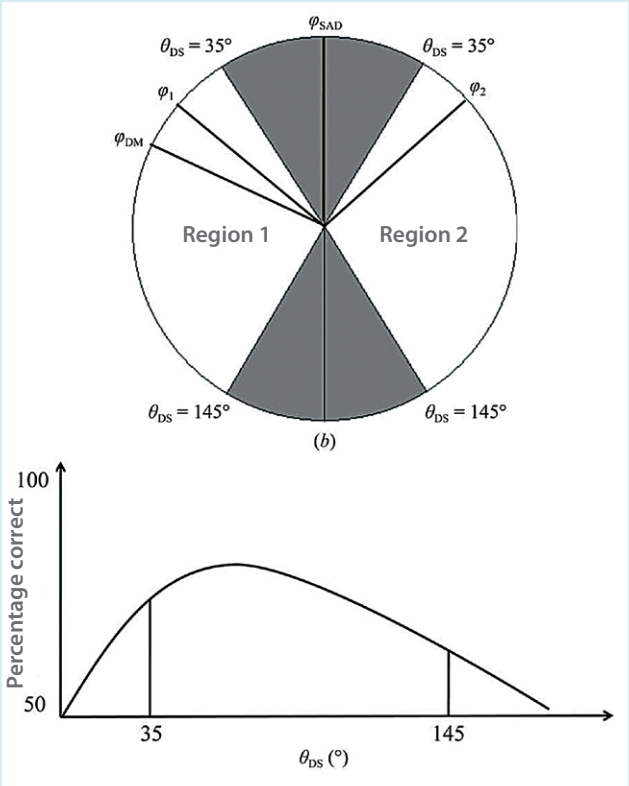

Fig. 2: (upper panel) Diagram of various phases and the range. The circle is divided into grey and white. Angles < 35° and > 145° in the grey zone show a smaller fraction correct in selecting phase φ_1 or φ_2 in region 1 or 2. (bottom panel) Schematic plot of histograms of the fraction correct as a function of angle ϕ_{DS}. (Reproduced from Ref. 3)

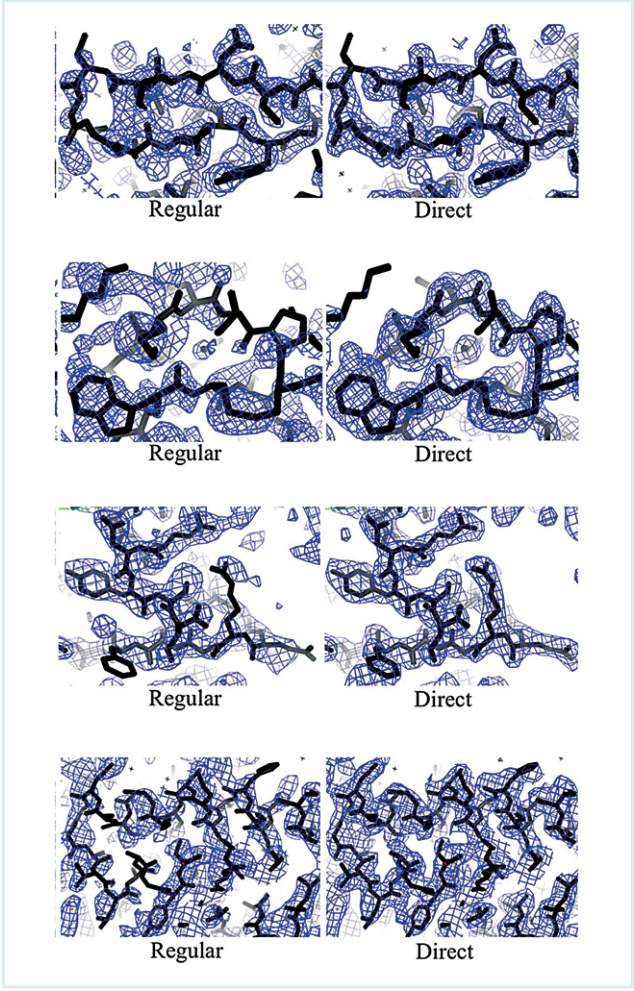

Fig. 3: Electron-density maps of lysozyme_Gd, lysozyme_S, insulin_S and HptB_Se (unknown structure) from the regular method and the direct selection method are shown with the same contour level 1.0σ in blue. The structures are shown as black sticks. (Reproduced from Ref. 3)

of the correct selected phase ϕ_{am}. The selected phase ϕ_{am} is either ϕ_1 or ϕ_2 , depending on the preliminary DM phase ϕ_{DM}^{NHL}. A portion of initial phases ϕ_{SAD} is then replaced correspondingly with these selected phases ϕ_{am}. All reflections with angle ϕ_{DS} in a range 35–145° are selected for an optimized improvement. The reflections with replaced phases (selected phases ϕ_{am}), and the rest with unselected initial phases ϕ_{SAD} are subsequently combined into a new data set with optimum initial phases ϕ_{SAD}^{S}.

A comparison of the conventional maps (the regular maps) and the direct-phase selection maps in all test cases shows that the continuity and completeness of the electron-density maps using the direct-phase selection method are significantly improved, and superior to those of conventional maps (Fig. 3). As a result, the completeness of auto-built residues with main chains and side chains in proteins with the direct-phase selection method is greater than that with regular methods. The map correlation coefficients and mean phase errors are generally improved by 0.05–0.2 and 10–18°, respectively, using the direct-phase selection method with a single cycle utilizing the new selected phases ϕ_{am}(ϕ_1 or ϕ_2), with a greater confidence level, to replace the corresponding initial SAD phases ϕ_{SAD}.

Their new direct phase-selection method provides a powerful protocol with an essential selection step, combined with current software of structure determination, such as *SOLVE/RESOLVE* and *CCP4*, to resolve the initial phase ambiguities of partial reflections for further

density modification. The resulting final DM phases and the electron density maps are improved effectively by the direct-phase selection method, compared with the regular methods, to yield improved statistical indicators of map quality and the completeness of model building for an efficient structure determination.

References

1. W. A. Hendrickson and M. M. Teeter, Nature **290**, 107 (1981).
2. Z.-J. Liu, E. S. Vysotski, C.-J. Chen, J. P. Rose, J. Lee, and B.-C. Wang, Protein Sci. **9**, 2085 (2000).
3. C.-D. Chen, Y.-C. Huang, H.-L. Chiang, Y.-C. Hsieh, P. Chuankhayan, and C.-J. Chen, Acta Cryst. **D70**, 2331 (2014).

Crowning Proteins: Modulating the Protein Properties Using Crown Ethers

*This report features the work of Cheng-Chung Lee, Manuel Maestre-Reyna, Andrew H.-J. Wang and their co-workers published in Angew. Chem. Int. Edit. **53**, 13054 (2014).*

Although protein X-ray crystallography is the main path to obtain structural information about proteins, protein crystallizability is still the main bottleneck in efforts on structural genomics. An optimization of crystallization is typically achieved on only a basis of case by case, trial and error. In contrast, on first identifying a ring-shaped binding mode for low-molecular weight polyethylene glycol (lmw PEG) in several protein crystal structures, Andrew H.-J. Wang and his co-workers established crown ether (18-crown-6; CR) as a reliable additive for crystallization and a powerful tool for crystallization. Their work shows that crown ethers can modify greatly the surface behavior of a protein by stabilizing either intra- or intermolecular interactions. Crown ethers can serve to modulate the diverse behavior of protein surfaces beyond crystallization, such as oligomerization, domain-domain interactions and stabilization in organic solvents.

As a basis to establish CR as surface modulator, they studied CR structural analogues, lmw PEG (MM < 600 g/mol). In protein co-crystal structures, these show two distinct conformational types—linear lmw PEG presenting an extended conformation and ring-shaped lmw PEG with a conformation similar to the CR structure. In the latter type, they typically make van der Waals (vdW) contacts with aromatic or aliphatic residues, or they coordinate primary amines (lysine) or guanidinium moieties (arginine) (Fig. 1(a)). They showed also that 68% of all deposited ring-shaped lmw PEG, but only 58% of linear PEG, mediated protein–protein contacts in the crystal. These observations indicate that CR, having physicochemical properties similar to those of lmw PEG, might be more constrained and hence better chelators and vdW partners for protein surfaces.

To investigate the effects of CR in protein crystallization, they performed sparse-matrix crystallization screening on several protein targets—Pin1R14A, DMP19, Rbma, SARS-CoV 3CL protease, lysozyme, myoglobin, and trypsin—based on common commercially available conditions. We found that CR affected crystal growth positively in most cases, with an exception of trypsin.

On solving the structures of all crystals obtained in the presence of CR, they observed the direct interactions with it in crystals of DMP19, Pin1R14A, hemoglobin and RbmA. In the latter, CR improved the crystal quality and resolution, making it possible to solve the complicated structure. In contrast, the DMP19, Pin1R14A and hemoglobin structures presented novel CR interactions with common characteristics (Fig. 2). Three distinct CR interaction modes comprise the K-crown, the C-crown and the KC-crown modes. In the first, it interacts with proteins in a similar fashion to ring-shaped lmw PEG on

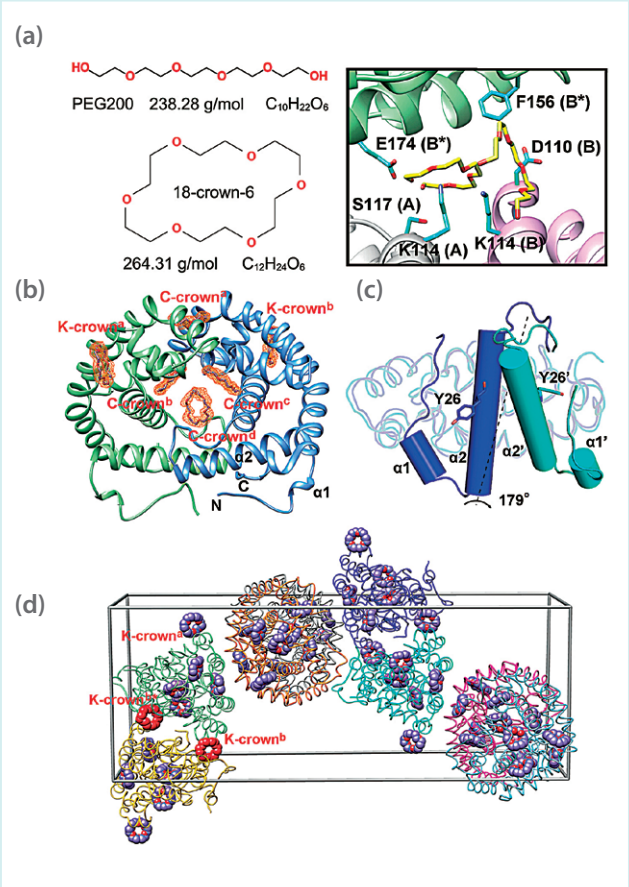

Fig. 1: PEG and 18-Crown-6 binding modes in a protein. (a) Top: PEG 200 in its linear conformation. Bottom: 18-crown-6 ether as a circular molecule. Right: Examples of lmw PEG adopting a ring-shaped conformation in various deposited crystal structures. dTMP kinase (2PLR) containing ring-shaped lmw PEG. (b) Structure of the DMP19•CR dimeric complex. Four C-crowns (C-crown^{a-d}) and two K-crowns (K-crown^a and K-crown^b), in purple, bind each DMP19 dimer (green and blue). (c) Comparison of monomers of the published DMP19 structure (3VJZ, in blue) and the DMP19•CR complex (cyan). The region between the N-terminus and α-helix 2 alters greatly, rotating by 179°. (d) Crystal packing of DMP19 and CR (purple sphere). The two CR molecules interacting across separate unit cells, K-crown^b and K-crown^{b*}, are shown in red.

coordinating the positive charge of a lysine axially (Fig. 2(a)). In the second, it stacks laterally either with aromatic and hydrophobic amino acids, or, via π-stacking, with carboxylic and guanidinium groups, which can clamp the CR (Fig 2(b)). The third binding has a mixed form, sharing characteristics of both the K- and C-crowns (Fig. 2(c)). As shown in Fig. 1(c), DMP19 revealed a new dimeric form containing in total six CR molecules, which caused α-helices 1 and 2 to rotate by 179° relative to the apo-structure. As the native dimeric state of DMP19

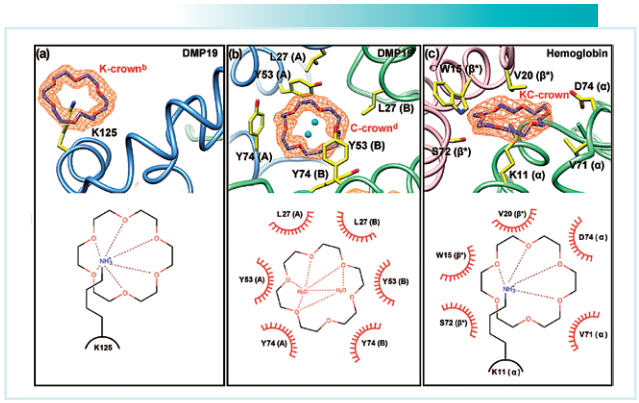

Fig. 2: 18-Crown-6 binding modes. The upper part of each panel illustrates the structure of the molecule; the lower part is a representation in which dashed lines represent hydrogen bonds and red semi-circles are hydrophobic contacts. (a) In the K-crown binding mode, a single lysine binds the CR axially. (b) Hydrophobic and p-orbital-containing side chains interact laterally with CR. No residue interacts with the central region of CR, which commonly, but not invariably, coordinates two water molecules. Letters in parentheses indicate the chain ID. (c) In the mixed KC-crown binding mode, the CR is coordinated axially with a lysine; hydrophobic and p-orbital-containing side-chains interact with it laterally. Letters in parentheses indicate the chain ID, with an asterisk indicating symmetry equivalents.

is the active conformation, they suggest that CR might interfere with the DMP19 function on altering its tertiary and quaternary structure.

In summary, the authors found that, on producing complexes, CR modified the properties of a protein surface, which resulted in alternative tertiary and quaternary structures. CR also increased the protein rigidity and, by CR–CR stacking, mediated direct interactions between hydrophobic patches and charged amino acids. They hence propose that CR, through its ability to modify protein surfaces, can serve in protein crystallography as a powerful additive, molecular probe to search for potential binding pockets, and reporter of protein conformational changes.

References

1. C.-C. Lee, M. Maestre-Reyna, K.-C. Hsu, H.-C. Wang, C.-I. Liu, W.-Y. Jeng, L.-L. Lin, R. Wood, C.-C. Chou, J.-M. Yang, and A. H.-J. Wang, Angew. Chem. Int. Edit. **53**, 13054 (2014).
2. M. Maestre-Reyna, W.-J. Wu, and A. H.-J. Wang, PLoS ONE **8**, e82458 (2013).
3. H.-C. Wang, T.-P. Ko, M.-L. Wu, S.-C. Ku, H.-J. Wu, and A. H.-J. Wang, Nucleic Acids Res. **40**, 5718 (2012).